Effects of precipitation behaviors on the microstructure and fracture toughness of Al-Cu-Mg aluminum alloys

Y. ZHAO[a], C. C. WANG[b], X. WANG[a,c,*], J. C. HUANG[c], G. F. ZHANG[a], M. T. WANG[a], Z. C. ZHANG[a], M. WU[a]
[a]*School of Mechanical Engineering, Liaoning Shihua University, Fushun 113001, P. R. China*
[b]*School of Materials Science and Engineering, Tsinghua University, Beijing 100084, P. R. China*
[c]*Department of Materials and Optoelectronic Science, National Sun Yat-Sen University, Kaohsiung 804, Taiwan, R. O. China*

In this paper, the effects of microstructure on fracture toughness were studied in Al-Cu-Mg alloy, including 2024 and 2124. As the ratio of Cu and Mg was similar in both alloys, the impurity elements in 2024 would lead to the formation of $A1_6$(Mn,Fe) and Al_7Cu_2Fe phases, which could affect the tensile strength and fracture toughness of the alloy. With the high Si content in 2024, θ (Mg_2Si) phase formed in matrix would impose negative factor in decreasing the mechanical property.

(Received July 15, 2015; accepted August 3, 2016)

Keywords: Aluminium alloy, Precipitation, Fracture Toughness, Microstructure

1. Introduction

In the past decade, the 2024 aluminum alloy series has been one of the most widely used Al-Cu-Mg alloys. The 2024 aluminum alloy has received considerable attention due to its high specific strength, good fracture toughness and excellent fatigue properties for structural materials applications in the automobile, aerospace and electrical cable industries [1-6]. In the early part of the last century, precipitation hardening was first discovered in an Al-Cu-Mg alloy. One of the most widely used alloys in the aeronautical industry was 2024 aluminum alloy that was introduced during World War II. To satisfy the practical requirements, experts put much emphasis on examining microstructure control as an alternative and viable means to enhance the mechanical properties [7-11]. Although different types of 2×24 (X=1-5) Al alloys were gradually developed, all of these alloys were designed based on 2024 Al alloy. Most studies investigated the content ratios of Cu and Mg and the impurity elements (Fe and Si). Researchers improved the mechanical properties of these alloys by using new heat treatments (deformation heat treatment), adjusting the contents of the alloy elements, adding alterants and refining the alloy [12-16].

For the Al-Cu-Mg alloy with high strength by aging strengthening, the main strengthen phase is the S phase. Initially, Bagaryatsky proposed a four-stage precipitation sequence for the ageing of Al-Cu-Mg alloys [17-19]:

$$SSS \rightarrow GPB\ zone \rightarrow S' \rightarrow S$$

This paper mainly discusses the microstructure and properties of Al-Cu-Mg alloys. The coarse phases and precipitated S phase that formed during the aging process were analyzed. The effect of the precipitated S phase in Al-Cu-Mg alloys on the mechanism of strengthening and toughening was discussed.

2. Experimental methods

The materials used in this investigation were the commercial 2024 and 2124 alloys with the chemical compositions listed in Table 1.

Table 1. 2024 and 2124 Alloy compositions (wt.%)

	Fe	Si	Cu	Mg	Mn	Al
2024	0.24	0.10	4.64	1.61	0.61	Bal.
2124	0.08	0.04	4.28	1.24	0.41	Bal.

The materials used for this work were parts of thin plates (material supplied by Northeast Light Alloy Co., Ltd). Samples of 2024 and 2124 aluminum alloy were solution treated at 495 °C for 1.5 h, quenched in room temperature water, and annealed at 190 °C for 12 h.

The morphology of the composite was observed by optical microscopy (OM, Neophot-I) and scanning electron microscopy (SEM, TESCAN VEGA 3). The microstructure was investigated by transmission electron microscopy (TEM, PHILIPS CM12) with a voltage of 120 kV. Discs with a diameter of 3 mm for TEM observation were placed

in a double jet polishing unit operated at 15 V and -20 °C with a 30% nitric acid and 70% methanol solution.

Tensile tests were conducted using an Instron 5569 universal electronic tensile testing machine with a crosshead speed of 1 mm/min at room temperature using a round bar specimen. The fracture toughness of compact tension (CT) specimens with a thickness (B) of 25 mm and a width (W) 50 mm were machined by extrusion in the L-T orientation. It should be noted that the specimen surface (L-T) was close to the extrusion surface. The fatigue load was applied at 50 Hz. For the fracture toughness testing, the length of the precrack was 2-4 mm. The tensile samples were tested using an Instron 5569 electronic tensile machine. The load was 30 kN, and the tensile rate was 2 mm/min. The samples for fracture toughness testing were in the plane strain state. The samples were taken from both the horizontal and vertical directions of the alloy board.

3. Results

3.1 OM observations

Fig. 1 shows the representative typical micrographs of the aluminum alloys in different rolling directions. Fig. 1 a), c), and e) are the L-S, T-L and T-S directions of the 2024 Al alloy, respectively. Fig. 1 b), d), and f) are the L-S, T-L and T-S directions of the 2124 Al alloy, respectively. The microstructure of both alloys was fully recrystallized. The grains were elongated in the L direction. The precipitated phases at the grain boundary of the 2124 alloy were in discontinuous distribution. However, the precipitated phases at the grain boundary of the 2024 alloy were relatively continuous. The coarse phases in 2024 were formed on the grain boundary as the chain structure. The content and size of these coarse phases in 2024 were relatively large. In the T-L direction, the content and size of these coarse phases were analyzed by statistical methods. The results showed that the content of these coarse phases in 2024 was approximately 10%. The size of these coarse phases was approximately 12.5 μm. The content of these coarse phases in 2124 was approximately 3.6%, and their size was approximately 9.5 μm. The content of impurity elements (Fe and Si) for both alloys was similar; however, the content and size of the coarse phases greatly differed.

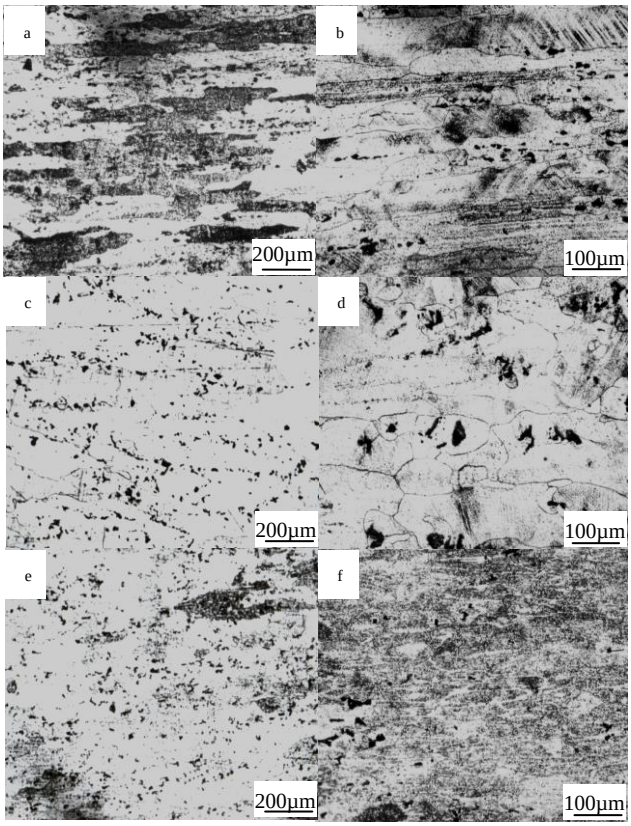

Fig. 1. Optical micrographs of the 2024 and 2124 alloys. a) 2024 (L-S) b) 2124(L-S) c) 2024 (T-L) d) 2124(T-L) e) 2024 (T-S) f) 2124(T-S)

3.2 TEM characterization

Fig. 2 shows the TEM observation for these two alloys after 12 h of aging. In Fig. 2, a large amount of needle-like precipitated phases were observed in both alloys. Because the S and S′ phases were identical in their chemical compositions and crystal structures, they differed only slightly in their lattice parameters. Additionally, there was a relationship between the crystal orientation of the matrix and the S and S′ phases. Fig. 2 c) and d) show that the content of these needle-like precipitated phases was relatively large in the 2124 alloy, and their distribution was uniform. However, Fig. 2 a) and b) show that the content of these needle-like precipitated phases was relatively small in the 2024 alloy, and their distribution was not uniform. The content of the impurity element Si was larger in 2024 than in 2124, and it formed a θ phase (Mg_2Si) with the Mg elements in the alloy. Therefore, the Mg_2Si content was larger in 2024 than in 2124; however, the content of the S phase was smaller in 2024 than in 2124. Both the S and θ phases were the main strengthen phases after peak aging; however, their strengthen abilities greatly differed. Fig. 2 b) and d) show that large precipitate phases were formed on the grain boundaries. The precipitated phases that formed on the grain boundary were lath-shaped and in discontinuous distribution on the grain boundary. The precipitated phases that formed on the grain boundary of

2024 were in continuous distribution, and their content was larger than that in 2124. The precipitated phases that formed on the grain boundary would significantly affect the fracture toughness of the alloy, and this effect was discussed in the next part of this paper. Fig. 2 b) and 2 d) show the small precipitated phases that formed within the grain and along the sub-boundaries. These phases would pin the dislocation and sub-boundary. Therefore, these phases could inhibit the movement of the dislocation and improve the stability of the sub-structure.

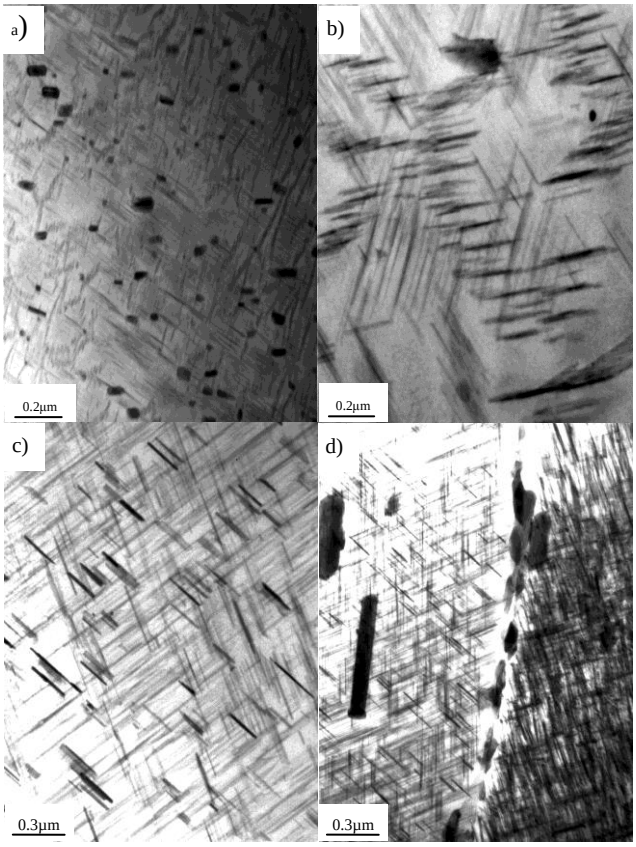

Fig. 2. TEM images showing the microstructure. a) ageing at 190 °C for 12 h of 2024 alloy b) ageing at 190 °C for 12 h of 2024 alloy c) ageing at 190 °C for 12 h of 2124 alloy d) ageing at 190 °C for 12 h of 2124 alloy

3.3 Fracture toughness

Fracture toughness testing was performed on the 2024 and 2124 alloys. The results showed that the fracture toughness of 2024 was much lower than that of 2124. The fracture toughness of 2124 in the L direction was 34-36 MPa•$m^{1/2}$, and the fracture toughness in the S direction was 29-32 MPa•$m^{1/2}$. However, the fracture toughness readings of 2024 in the L and S directions were 26-28 MPa•$m^{1/2}$ and 23-25 MPa•$m^{1/2}$, respectively.

Fig. 3 shows representative typical crack fracture micrographs of the two alloys. The observed fracture results are shown in Fig. 3. Fig. 3 a) and b) show that the upper half of the alloy exhibits cleavage fracture. The fracture picture showed that the river pattern and the interface between the crack and the fracture zone could be observed. Fig. 3 c) and d) show typical dimple fracture. The fracture contained many large holes and small dimples. In addition, a shear lip and equiaxed dimple could be observed. Some precipitated phases could be observed in the center of the dimple. There were also some parabolic dimples, which were small in size, in the shear lip. The fracture of both alloys was multiple fracture. The size of the precipitated phases in the dimples and the amount of dimples in 2124 was smaller than those in 2024. Fig. 3 e) and f) show the entire precipitated phases or part of the precipitated phases in the large dimples. The precipitated phases in a chainlike distribution in the dimples of 2024 were consistent with the observed results in the metallographic photos.

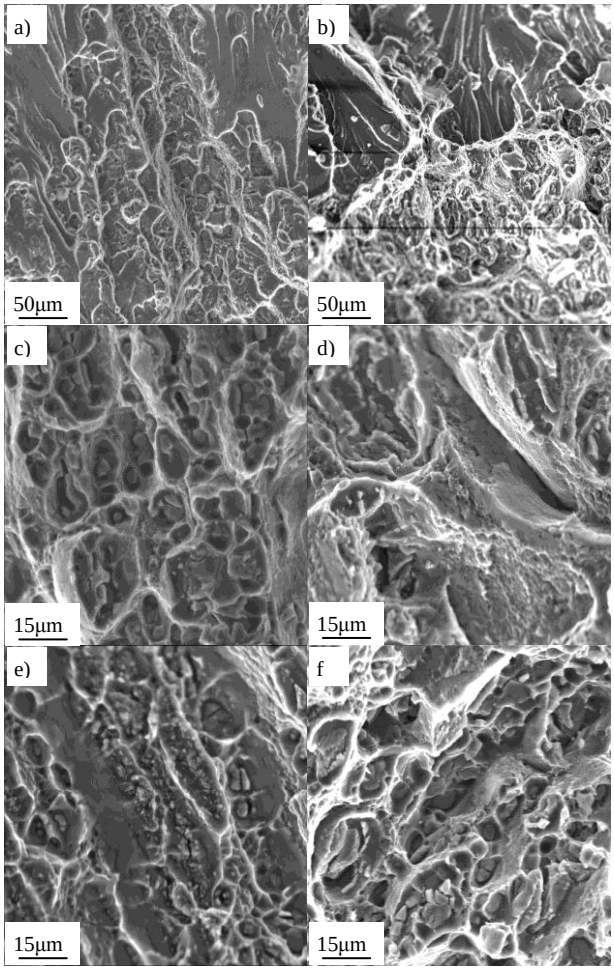

Fig. 3. The crack fracture surface after test on aluminum alloy. a) the crack front geometry at the fringe region on 2024 alloy b) the crack front geometry at the fringe region on 2124 alloy c) fringe region on 2024 alloy d) fringe region on 2124 alloy e) precipitated phases in chainlike distribution in 2024 and their destruction f) fracture caused by precipitated phases in 2124

4. Discussion

There were many factors that could affect the fracture toughness of the alloy, including the structure of the grain, the content of the coarse phase, the precipitated phases on the grain boundary, the PFZ and the state of precipitated phases in the matrix [20, 21]. As the results showed in the previous sections, the effect of the coarse phases on the fracture toughness was significant, and the aging state of the alloy was also important. In this paper, the effects of the coarse phases and aging state on the fracture toughness were mainly discussed.

4.1 Coarse phases

Fig. 1 shows that the content and size of the coarse phases were larger in 2024 than those in 2124. The content and size of the coarse phases had a great relation with the composition and casting process of the alloy. If the cooling rate was not controlled well and the homogenization was not perfect during the casting process, a coarse dendrite network would form. If the carbide was not destructed during the rolling process or the carbide could not dissolve in the alloy during the solid solution treatment, coarse phases would form in the alloy. The SEM results showed that the coarse phases contained Fe and Si and formed $A1_6$(Mn, Fe) and Al_7Cu_2Fe. Many studies showed that these coarse phases decreased the alloy's ability of local plastic deformation because of their poor shape and large volume. Therefore, the crack would easily expand. When the content of impurity elements in the alloy was large, the crack formed along the chain of the coarse phases and decreased the fracture toughness of the alloy. Therefore, it was important to control the content of impurity elements in the alloy. On the one hand, for this purpose, we can improve the purity of raw materials, and optimize the casting process for the other hand.

4.2 Effects of aging on the mechanical properties

Fig. 4 shows the tensile strength of the alloys in solid solution, 9 h aging and 12 h aging states. The results showed that the strength of 2024 was lower than 2124 in all of the states. Fig. 5 shows the fracture picture of 2124 in solid solution and 12 h aging states. Fig. 5 a) shows that the fracture was along the grain boundary, caused by the coarse phases. The dimple was shallow, and some large precipitated phases were observed in the dimples. Fig. 5 b) shows the fracture picture of 2124 in the 12 h aging state. The fracture was a combination of intergranular fracture and dimple fracture. Some studies reported that when the aging state was peak aging, the precipitated phases on the grain boundary grew, the precipitate-free zone became wide, and the grain boundaries became weak. In this situation, the dislocation could still cut through the precipitated phases and form a shear deformation zone. However, when the shear deformation zone met the dislocation, a strain concentration formed on the grain boundary, which weakened the grain boundary and formed the crack. Especially for the precipitated phases formed on the grain boundary, they could lead to intergranular fracture.

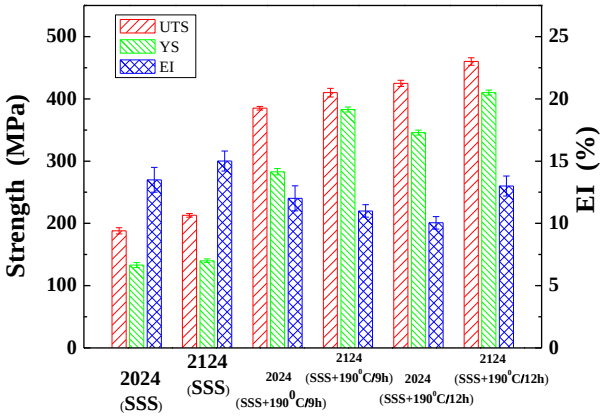

Fig. 4. Changes of tensile properties of alloy ageing at various time

4.3 Precipitation behaviors

Many studies showed that when the ratio of Cu/Mg was between 1.5 and 4, the main aging precipitate in Al-Cu-Mg alloys was the S phase (Al_2CuMg), which was the equilibrium phase that exhibited good high-temperature strength [22].

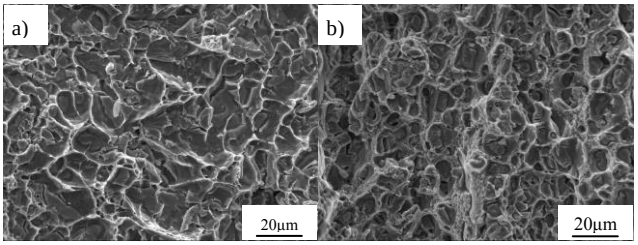

Fig. 5. SEM micrographs of the fracture surface the 2124 alloy. (a) SSS (b) SSS+190°C/12h

Fig. 6 shows the TEM observation results of 2124 in the solid solution state. It was clear that the dislocation density was low and that the precipitated phases formed unevenly. The large rod-like dispersoids were identified as the orthorhombic T phase ($Al_{20}Cu_2Mn_3$). The length-to-diameter ratios for these phases were 1-6. For the GPB zone, the lattice misfit between the GPB zones and the aluminum matrix was very small. Therefore, it was extremely difficult to observe the GPB zone. Nevertheless, the aging time enhanced the nucleation of precipitates, which accelerated the precipitation of GPB zones.

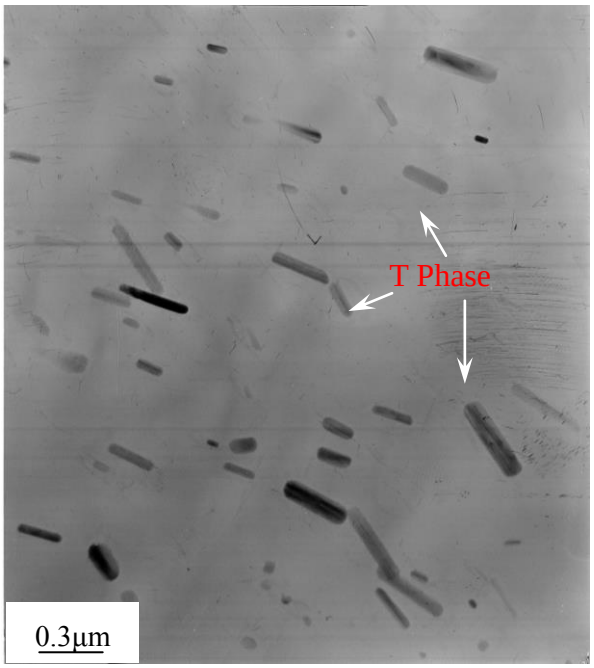

Fig. 6. The TEM observation of 2124 in solid solution state.

Fig. 7 shows the TEM observation results of 2124 in the 1 h aging state. The TEM micrographs in Fig. 7 a) were taken near the [001] zone axis. The dislocation density was high. There were also some small particles in the S′ phase (GP2 zone). The dislocation distribution was uneven (Fig. 7 b)). These remnant T-phase particles played a critical and positive role in grain refinement and dislocation accumulation.

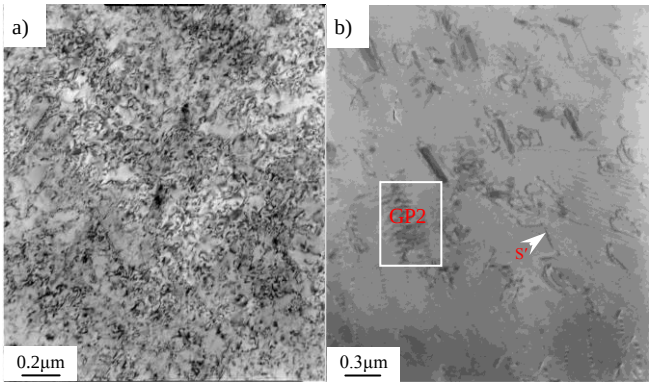

Fig. 7. The TEM micrographs of 2124 in 1h aging state. a) TEM micrographs were taken near the [001] zone axis b) S′ and GP2 zone

Fig. 8 shows the TEM observation results of 2124 in the 9 h aging state. Fig. 8 a) shows that precipitate-free zone on the grain boundary became wide during the aging process. Fig. 8 b) and c) show the formation of S′ phases in lamellar shapes, and the disappearance of the GP zone. The content of S′ phases was small. Therefore, the mechanical properties were not as good as those in the peak aging state.

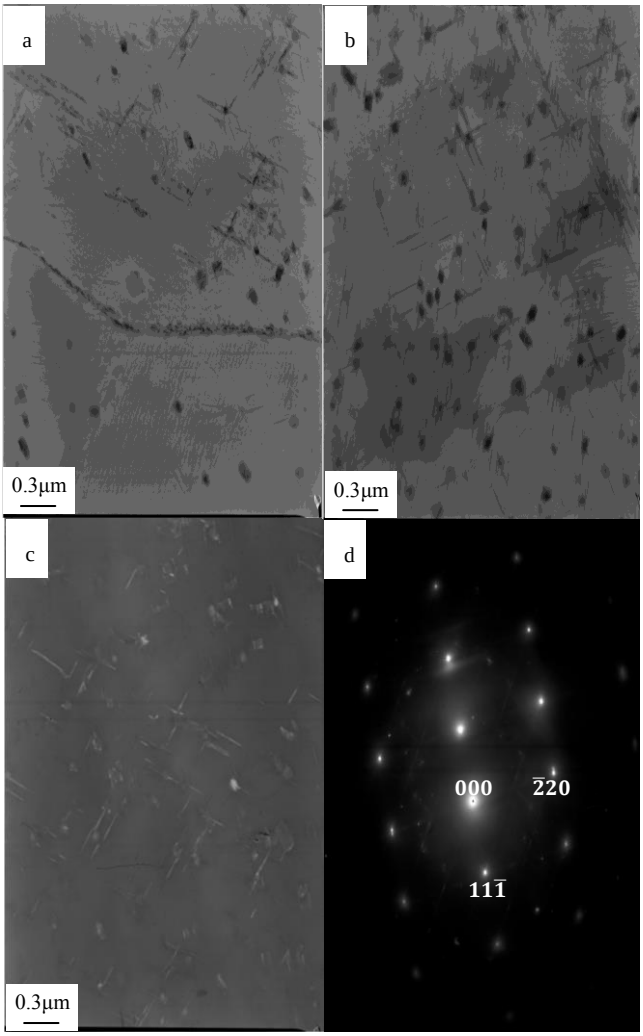

Fig. 8. The TEM micrographs of 2124 in 9h aging state a) bright-field image b) bright-field image 120 °C/9h c) dark-field image 120 °C/9h d) SAED patterns of samples aged 〈112〉

At the beginning of the aging, the GP zone formed uniformly in the matrix. The GP zone was the segregation of solute atoms in the matrix phase lattice. Because of the difference in the atomic radius between the solute atoms and solvent atoms, a strain field would form around the GP zone. When the dislocation moved to the GP zone, it could cut through the GP zone, and at that time, there would be an interaction between the strain field and the dislocation strain field, which could inhibit the dislocation movement.

When the alloy was in the peak aging state, the relationship between the S phase and the matrix was semi-coherent. The S phase had larger lattice distortion than the GP zone, and the S phase had larger effect on inhibiting the dislocation movement. In addition, the crystal structure of the S′ phases was FCC, which was different than the matrix; therefore, there would be energy consumption when the dislocation cut through the S′ phases. The energy consumption contained two parts: (1) chemical hardening caused by the increase of the interface and (2) the stacking

fault energy enhancement caused by the difference of the modulus. Therefore, the dislocation cutting through the S′ phases had larger energy consumption than cutting through the GP zone, and the mechanical properties of 2124 were better than 2024 with the help of the S′ phases.

Hornbogen and Graf modified the equation for calculating fracture toughness, which was first established by Hahn-Rosefield [23-25]. The modified equation is shown below:

$$K_{IC} = (L \cdot E \cdot \sigma_{yi} \cdot n_i^2 \cdot \varepsilon_{fi} \cdot W / D)^2$$

Where K_{IC} ---- fracture toughness
L ---- experience parameter
σ_{yi} ---- yield stress
n_i ---- work hardening exponent
ε_{fi} ---- critical fracture strain for the PFZ zone
w ---- width of PFZ zone
D ---- grain size

From this equation, it was clear that the strain concentration at the PFZ zone would lead to a decrease in the fracture toughness.

For the intergranular fracture in the aging state, planar slip during the process of deformation of the matrix played an important role. The slip was on the narrow deformation sliding band, which would lead to the strain concentration on the grain boundary and the crack along the grain boundary. Planar slip and stress concentration on the grain boundary would lead to intergranular cracking. However, slipping through the grain boundaries could also release the stress concentration and inhibit the intergranular cracking. Therefore, the planar slip would lead to intergranular cracking only when the grain boundary was weak, for example, when the precipitated phases formed on the grain boundary. The slipping usually formed at the {111} plane. For the peak aging or over aging states, the effect of planar slip on intergranular cracking was not significant. Therefore, the dislocation usually bypassed the precipitated phases. The intergranular cracking was mainly caused by the strain concentration on the PFZ zone.

The crack caused by the coarse phases existed in all of the aging processes. In the over aging state, all of the cracks were caused by the coarse phases, which could also be observed in the under aging and peak aging processes. The dimple fracture caused by the coarse phases played an important role in the fracture toughness of the material. For the brittle particle Al_7Cu_2Fe, it would cause cracking at the beginning of the plastic deformation and form a crack source. However, this process was far from the macro fracture of the material.

The effect of aging on the fracture mode was complicated. With the increase of aging time, the ductility of the shear fracture decreased and the intergranular fracture and dimple fracture increased. The possibility of intergranular fracture became the largest in the peak aging state. Then, the possibility of intergranular fracture decreased during the over aging process, and the dimple fracture increased.

The factors that could affect the fracture toughness included the yield strength, the plastic properties of the matrix and the microstructure on the grain boundary. The yield strength was the largest in the peak aging state. The work hardening rate became larger during the under aging process. The precipitated phases grew with the increase in aging time. In the over aging state, the most important factors were the strength of the matrix and the change of the precipitated phases

5. Conclusions

In this paper, the effect of aging precipitation on fracture toughness was studied in two different Al alloys, including Al 2024 and Al 2124. Al 2024, which had a higher content of impurity elements, had lower tensile strength and fracture toughness than 2124, which was mainly caused by the Al_7Cu_2Fe phases in the matrix. Therefore, it was very important to control the content of the impurity elements. With the increase in aging time, the mechanical properties of the alloys increased. When the two alloys were in the peak aging state, the main precipitations in 2124 were S′ and S. The main precipitations in 2024 were also the S′ and S phases; however, the θ phase, which affected the mechanical properties, also formed in 2024.

Acknowledgments

This research was supported by the National Natural Science Foundation of China (Grant No. 51574147) and Project Supported by Scientific Research Fund of Liaoning Provincial Education Department, China (No. L2014154).

References

[1] Y. L. Zhao, W. W. Hu, Z. Q. Yang, Micron. **76**, 1 (2015).
[2] W. C. Wu, Y. J. Wang, J. B. Wang, S. M. Wei, Mater. Sci. Eng. A **608**, 190 (2014).
[3] S. C. Wang, M. J. Starink, Acta. Mater. **55**, 933 (2007).
[4] S. C.Wang, M. J. Starink, N. Gao, Script. Mater. **54**, 287 (2006).
[5] Z. L. Hu, X. S. Wang, S. J. Yuan, Mater. Charact. **73**, 114 (2012).
[6] P. K. Rout, M. M. Ghosh, K. S. Ghosh, Mater. Charact. **104**, 49 (2015).
[7] A. Wiengmoon, Pearce, T. H. John, T. Chairuangsri, S. Isoda, H. Saito, H. Kurata, Micron. **45**, 32 (2013).
[8] X. G. Fan, D. M. Jiang, L. Zhong, T. Wang, S. Y. Ren, Mater. Charact. **58**, 24 (2007).
[9] Y. C. Lin, Y. Q. Jiang, Y. C. Xia, X. C. Zhang, H. M. Zhou, J. Deng, Mater. Sci. Eng. A, **605**, 192 (2014).
[10] E. M. Elgallad, P. Shen, Z. Zhang, X. G. Chen, Mater. Design **61**, 133 (2014).

[11] Z. Q. Feng, Y. Q. Yang, Y. X. Chen, B. Huang, M. S. Fu, M. H. Li, J. G. Ru, Mater. Sci. Eng. A **586**, 259 (2013).
[12] D. R. Sun, X. C. Sun, D. O. Northwood, J. H. Sokolowski, Mater. Charact. **36**, 83 (1996).
[13] Z. Q. Feng, Y. Q. Yang, B. Huang, X. Luo, M. H. Li, Y. X. Chen, M. Han, M. S. Fu, J. G. Ru, Philosophical Magazine **93**, 1843 (2013).
[14] M. Murayama, K. Hono, Acta. Mater. **47**, 1537 (1999).
[15] P. I. Gouma, D. J. Lloyd, M. J. Mills, Mater. Sci. Eng. A **319-321**, 439 (2001).
[16] X. F. Xu, Y. G. Zhao, B. D. Ma, M. Zhang, J. Alloy. Compd. **610**, 506 (2014).
[17] C. M. C. Jimenez, O. A. Ruano, M. Carsi, F. Carreno, Mater. Sci. Eng. A **552**, 530 (2012).
[18] S. Cheng, Y. H. Zhao, Y. T. Zhu, E. Ma, Acta. Mater. **55**, 5822 (2007).
[19] M. J. Styles, C. R. Hutchinson, Y. Chen, A. Deschamps, T. J. Bastow, Acta. Mater. **60**, 6940 (2012).
[20] J. Z. Liu, S. S.Yang, S. B. Wang, J. H. Chen, C. L. Wu, J. Alloy. Compd. **613**, 139 (2014).
[21] H. C. Shih, N. J. Ho, J. C. Huang, Metall. Mater. Trans. A **27**, 2479 (1996).
[22] T. S. Parel, S. C. Wang, M. J. Starink, Mater. Design **31**, 2 (2010).
[23] M. Rashad, F. Pana, M. Asif, S. Hussain, M. Saleem, Mater. Charact. **95**, 140 (2014).
[24] B. Q. Li, A. P. Reynolds, J. Mater. Sci. **33**, 5849 (1998).
[25] G. T. Hahn, A. R. Rosenfield, Metall. Trans. A **6**, 653 (1975).

*Corresponding author: wx1979875@hotmail.com, wangxu@lnpu.edu.cn